



# SLHC-PP

## MILESTONE REPORT

### EU MILESTONE: 6.2

---

Document identifier: **SLHC-PP-M6.2-982402-v1.0**

Contractual Date of Delivery to the EC of **End of Month 10 (January 2009)**

Actual Date of Delivery to the EC of **August 2010**

Document date: **18/5/2009**

Milestone Title: **Basic Magnet design**

Work package: **WP6: Development of Nb-Ti quadrupole magnet prototype**

Lead Beneficiary: **CERN**

Authors: **F. Borgnolutti, P. Fessia and E. Todesco**

Document status: **Draft**

Document link: <https://edms.cern.ch/document/982402/1>

---



## Electromagnetic Design of the 120 mm Aperture Quadrupole for the LHC Phase One Upgrade

F. Borgnolutti, P. Fessia and E. Todesco

### Abstract

The phase I of the LHC upgrade aims at increasing the luminosity by a factor 2-3 with respect to the nominal luminosity of  $10^{34} \text{ cm}^{-2}\text{s}^{-1}$ . Part of this increase is obtained through a reduction of  $\beta^*$  from 55 to 25-30 cm. This requires the replacement of the present quadrupole triplets of 70 mm aperture around the Atlas and CMS interaction regions with a new set of Nb-Ti quadrupoles with 120 mm aperture. In this paper we present a proposal for the electromagnetic design of the coil cross-section and of the non-connection side of the coil ends. We also present an estimate of the field quality components, using the usual split among systematic, uncertainty associated to the systematic and random part.

CERN, Technology Department  
LHC IR Upgrade Phase I

I.	Introduction.....	3
II.	Electromagnetic design of the magnet cross-section.....	3
2.1.	Cable features .....	3
2.2.	Choice of the number of layers based on scaling laws.....	4
2.3.	Choice of the block angles based on a pure sector coil model .....	5
2.4.	Cross-section with Rutherford cables and iron.....	10
2.5.	Iron yoke.....	13
2.6.	Summary of magnetic performances .....	15
2.7.	Impact on the field quality of a thin slot in the yoke to improve the heat transfer.....	17
III.	The layer jump and splice.....	18
IV.	NCS coil end.....	19
4.1.	Geometry of the coil head.....	19
V.	Field quality .....	23
5.1.	Random component .....	24
5.2.	Systematic field harmonic errors .....	25
5.3.	Field error due a radial offset of the splice.....	29
5.4.	Field error due to longitudinal displacement of layers .....	30
5.5.	Magnetic field quality summary .....	30
5.6.	Fine tuning of the multipoles through mid-plane shims.....	32
VI.	Summary.....	33
	References.....	33

## I. Introduction

The phase I upgrade [1,2] of the interaction regions around the CMS and Atlas experimental areas requires the replacement of the triplet, presently made by the MQXA [3] and MQXB [4] 70 mm aperture quadrupoles built by the US-Japan collaboration, with a new quadrupole MQXC, using the same technology of Nb-Ti. This set of quadrupoles should have a larger aperture and longer length, thus allowing to squeeze  $\beta^*$  in the two interaction points up to 25-30 cm. The present lay-out of the optics is being finalized, and an aperture of 120 mm has been selected during an internal review of the project in July 2008 [2]. This corresponds to a length of the order of 10 m and an operational gradient of about 120 T/m at 1.9 K. It is foreseen to use the existing spare cable of the main LHC dipoles to both speed up the tight schedule and to reduce the costs.

We first present the main reasons for choosing a two-layer coil, on the basis of semi-analytical scaling laws. This option has been already considered in Ref. [1,5] for similar apertures. Then, we make an exhaustive scan through the possible four blocks, two-layers cross-sections providing acceptable field quality through a semi-analytical method based on sector coil. This method gives a hint on the coil angles providing the optimal lay-out. A realistic lay-out is then computed using the actual Rutherford cable. The choice of the coil cross-section is done in order to get both the largest short sample gradient, i.e. maximizing the operational margin, and to get a low operational current to fit with the constraints imposed by the existing equipment. Collars are assumed to be 35 mm large, on the ground of the choice of self supporting structure and mechanical computations carried out in a separate paper [6].

We then analyse the design of the iron yoke, taking into account the constraints set by the field quality and the hole needed for the heat exchanger. We assume that the field quality optimization has to be carried out only at high field: this considerably simplifies the yoke optimization. We then propose a design for the layer jump connecting the inner and outer layer, and the lay-out of the coil head in the non-connection side. For the coil head, a crucial point is the location and the value of the peak field.

We finally carry out the estimate of the expected field harmonics, separating the systematic part, the uncertainty associated to the systematic, and the random part. A summary table to be used as a first guess for the beam dynamics simulations is given.

## II. Electromagnetic design of the magnet cross-section

### 2.1. Cable features

The MQXC quadrupole magnet will use the same keystoneed Rutherford Nb-Ti cables (both inner and outer layer) as in the LHC main dipole [1]. The cable insulation will probably differ from the main dipoles: a new insulation scheme, allowing a direct path to helium from the bath to the strands has been proposed. This slightly changes the expected size of the insulation [8]. The main geometric and electric features of the cables are summarized in Table 1. The cables insulation thickness are obtained from the recent measurements performed on a stack of cables pressurized at 50 MPa. The inner and outer cables of the LHC main dipole are named cable 01 and cable 02 respectively, following the standard notations used for the LHC.

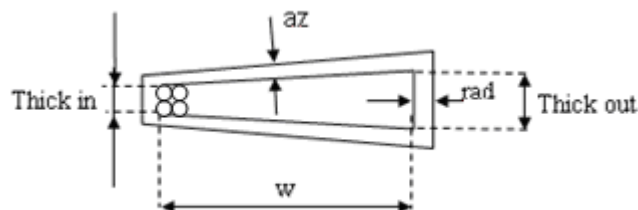


Fig. 1– Cable cross-section.

Table 1: Cables parameters, with porous insulation.

	unit	cable 01	cable 02
w	mm	15.100	15.100
thick in	mm	1.736	1.362
thick out	mm	2.064	1.598
Radial insulation	mm	0.160	0.160
Azimuthal insulation	mm	0.135	0.145
Number of strand		28	36
strand diameter	mm	1.065	0.825
Cu/Sc ratio		1.65	1.95
$I_{ss}$	A	14800 (10T)	14650 (9T)
$\Delta I_{ss}/\Delta B$	A/T	4680 (10T)	4050 (9T)
$j_{ss}$	A/mm <sup>2</sup>	1572 (10T)	2245 (9T)
$j_{ss}/\Delta B$	A/T/mm <sup>2</sup>	497 (10T)	620 (9T)

The cables 01 and 02 have a cross-sectional area (insulation included) of 33.4 mm<sup>2</sup> and 27.3 mm<sup>2</sup> respectively. Since the cables will be fed by the same current, this corresponds to a having a current density in the outer layer 23% larger than in the inner layer, i.e. a grading of 1.23, as in the LHC main dipoles. Cables 01 and 02 are available in unit lengths of 460 m and 780 m respectively: this constraint should be taken into account in the coil design. The superconducting performances of the cables are taken as the more pessimistic values derived from the more recent measurement performed at 1.9 K on the spare cables of the LHC main dipole (see Table 1).

## 2.2. Choice of the number of layers based on semi-analytical laws

Semi-analytical scaling laws developed in [9] allow estimating the short sample gradient of ironless quadrupoles as a function of the magnet aperture, of the coil width and of the superconducting cable short sample current. The short sample gradient versus the coil width curve plotted in Fig. 2 has been obtained by applying such a scaling law for a 120 mm quadrupole aperture, without grading and iron, with a Nb-Ti conductor similar to the LHC inner cables. The model relies on a hyper-simplified coil lay-out, made up of a 30° sector with uniform current density. According to Fig. 2, a one layer coil would give a short sample gradient of about 110 T/m. Adding a second layer, one can reach about 140 T/m, and a third layer would give 150 T/m. From this estimate, the increase of about 7% obtained by adding a third layer seems not reasonable. A two-layer coil looks as a good compromise in having a large gradient without using too much cable from the LHC spares.

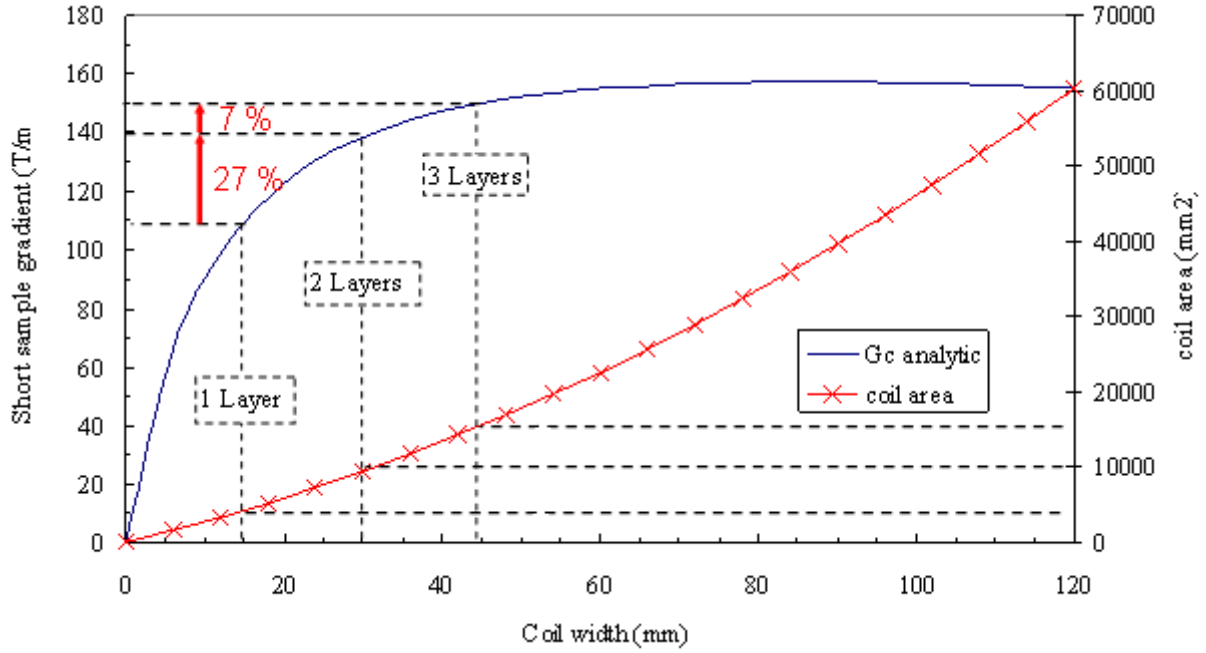


Fig. 2- Analytical estimate of the short sample gradient and coil area versus the coil width for an ironless 120 mm aperture quadrupole made with the LHC main dipole cables.

### 2.3. Choice of the block angles based on a pure sector coil model

Field quality imposes stringent constraints on the coil block positions and angles. The first orders harmonics  $b_n, a_n$ , with  $n < 10-15$  of the harmonic decomposition

$$B(z) = 10^{-4} B_2 \sum_{n=1}^{\infty} (b_n + ia_n) \left( \frac{z}{R_{ref}} \right)^{n-1} \quad (1)$$

must not be larger than one unit, (i.e.,  $10^{-4}$  of the main quadrupolar component). The coil symmetry sets automatically to zero all harmonics except the so-called ‘allowed’ harmonics  $b_6, b_{10}, b_{14}, \dots$ . Coils are made up of blocks which dimensions and position are chosen so as to minimize  $b_6, b_{10}$  and  $b_{14}$  (see Fig. 3) Higher order allowed multipoles are not taken into account because they are naturally small, due to the power law decay of Biot-Savart. A parametric study i.e. a complete scan over blocks dimensions and position cannot be performed due to CPU time limitations.

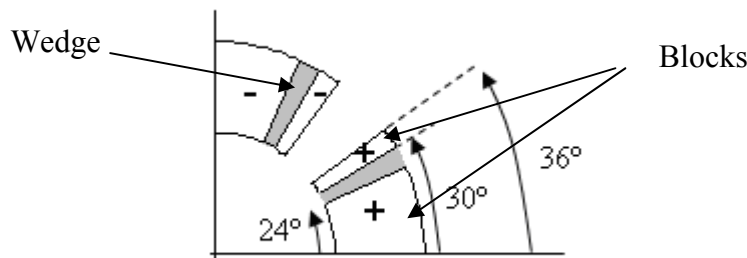


Fig. 3 – Quadrupole coil made of 2 blocks and one wedge allowing cancelling  $b_6$  and  $b_{10}$ .

Here we propose a different way to optimize the coil cross-section. In order to save CPU time, we allow less accuracy in the block description, namely we assume blocks as sector coils with uniform current density (see Fig. 4). This neglects the non-perfect cable keystoneing which leads to blocks whose shape is not a pure sector, as well as the slight current grading due again to the cable keystoneing. The sector approximation allows to express the magnetic field through explicit equations obtained from the Fourier decomposition. This model is fast to compute and thus allows making a exhaustive parametric study of coils having up to four blocks. Having selected the

solutions that satisfy the field quality constrain, we compute the short sample gradient, the short sample current and the magnetic forces acting on the coil. An unsaturated circular iron yoke is also taken into account by means of the imagine method. The distance between the yoke and the outer radius of the coil, which is the collar size plus a space gap of 2 mm, is set to 37 mm according to mechanical computations given in [6].

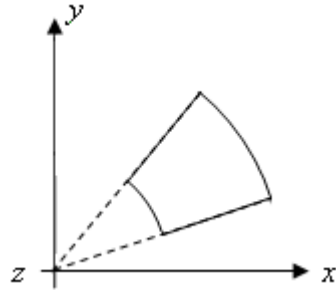


Fig. 4 – Pure sector coil block.

We showed in chapter 2.2. that the best coil lay-out option for a 120 mm aperture quadrupole magnet based on the LHC main dipole cables is a two-layer coil. One has to minimize the allowed multipoles  $b_6$ ,  $b_{10}$  and  $b_{14}$  while keeping a high short sample gradient. A three-block coil, i.e. a coil having only one copper wedge in the inner layer, would give four free parameters ( $\theta_1$ ,  $\theta_2$ ,  $\theta_3$  and  $\theta_4$  in Fig. 5 left). This is just enough to optimizing the three multipoles and the gradient. More flexibility comes from adding a second wedge in the outer layer, i.e. having a four-block coil, as for the LHC MQ or MQXB; this gives 6 angles as free parameters (see Fig. 5 right).

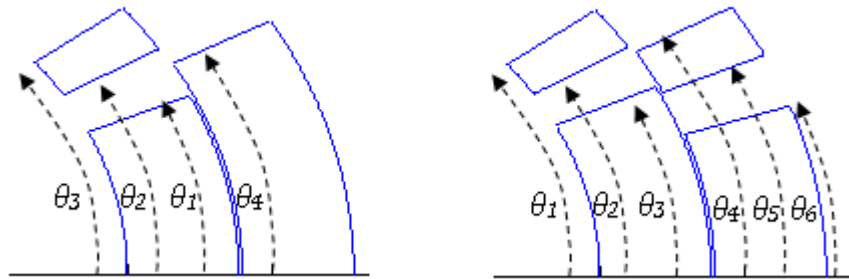


Fig. 5- Cross-section of the 3 (left) and 4 (right) blocks coil considered in the semi-analytical search for the optimal coil lay-out.

Multipoles are analytically computed through the Fourier transform method. An example of the magnetic flux evaluated through this method for one of the analysed cross-sections shown in Fig. 6. The scan on the six-dimensional parameter space is done in the following way

- The angular step of the six variables (angles) is set to  $0.1^\circ$ .
- The maximal angular dimension of the coil has been set to  $41^\circ$ , providing a collar nose thickness at least as large as what used in the LHC main dipole.
- The scan is done through all the possible combinations.
- Multipoles are computed at  $2/3$  of the aperture radius (40 mm), and the set of angles giving the absolute value of the first three allowed multipoles ( $b_6$ ,  $b_{10}$  and  $b_{14}$ ) below 1 unit are kept.

For the solutions satisfying the field quality constraints, we computed the short sample gradient and current, the magnetic forces acting on the coil, and the amount of cables used. The next step is to sort these solutions out according to the gradient value, to the amount of cable used or to the mechanic feasibility of the coil.

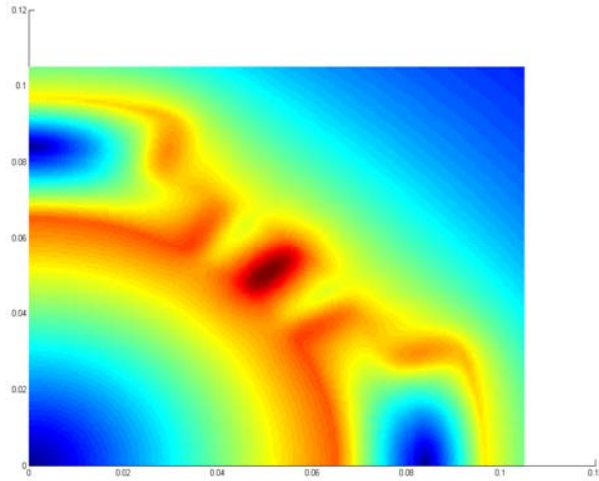


Fig. 6 - Magnetic flux density computed by means of the analytical model.

We first consider two different arrangements of the cables 01 and 02. The first arrangement is called “normal grading” and consists in winding the outer layer exclusively with the cable 02 and the inner layer exclusively with the cable 01 (Fig. 7 right). The second arrangement is named “special grading” because the cable 01 which has the lowest current density (yellow cable) is not only used to wind the layer 1 but also to wind the upper block of the layer 2 (Fig. 7 left). Here we make a parametric study based on analytical equations derived from Fourier decompositions of the coil to determine what would be the possible gain on the gradient due to a special grading of the magnet coil. A scan of all the possible coil blocks angular thickness and position satisfying the field quality requirement set in 3.1 for both the normal grading and special grading led to the 3D plot in Fig. 8 where the short sample gradient is plotted versus the length of the cable 01 and cable 02 needed to wind one pole (head excluded). 2D plots of the same variables are shown in Fig. 9 and in Fig. 10. Each marker is a cross-section satisfying the field quality requirement. Around 150 cross-sections with good field quality are plotted. One can draw the following conclusions.

- The largest short sample gradient is around 150 T/m, to be compared to the previous estimate of 140 T/m, which neglected both the iron and the grading effect.
- Both special grading and normal grading have similar maximal gradients (within 1%).
- There is a large number of solutions with special grading using much more cable 01: these are not so interesting in our case, since the unit length of the cable 01 is pretty short (see Fig. 9).

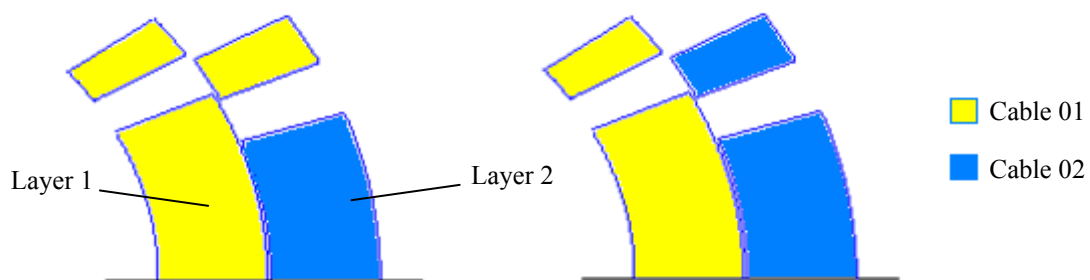


Fig. 7- Special grading (left) and normal grading (right) schemes. The colour blue indicates the cable 02, and the yellow the cable 01.



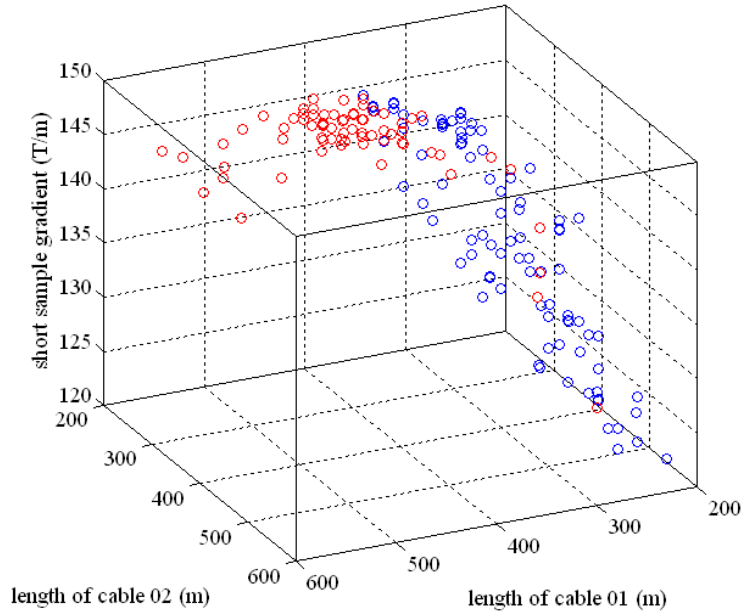


Fig. 8 – Short sample gradient versus length of cables 01 and 02 needed to wind one pole. Red markers correspond to special grading cases and blue markers to normal grading cases.

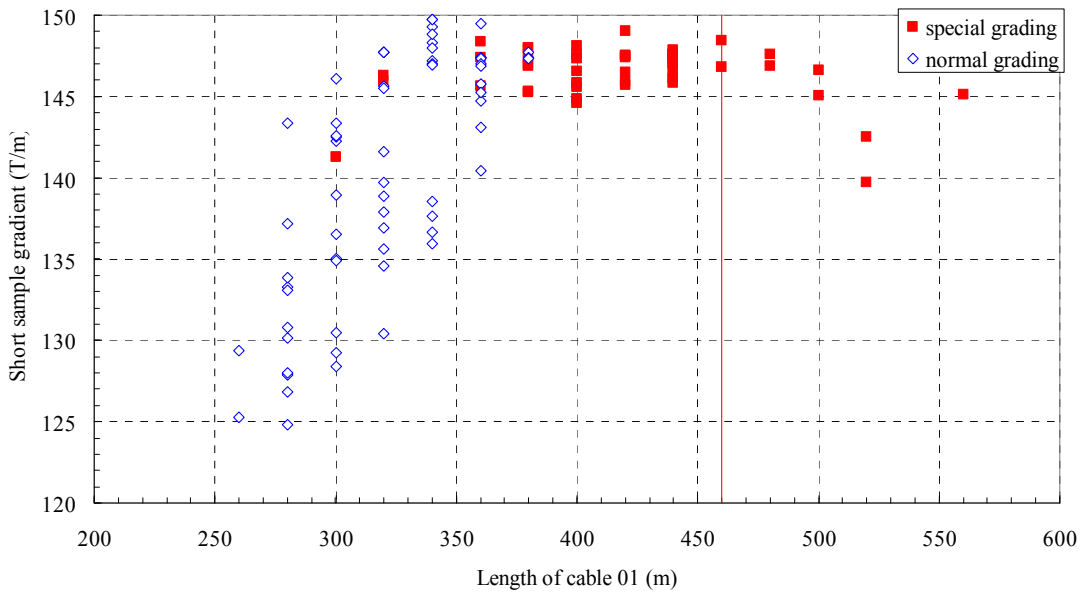


Fig. 9- Short sample gradient versus the length of the cable 01 needed to wind one pole (head excluded) for the normal grading (empty markers) and for the special grading (red marker). The red line is the unit length of cable 01 available.

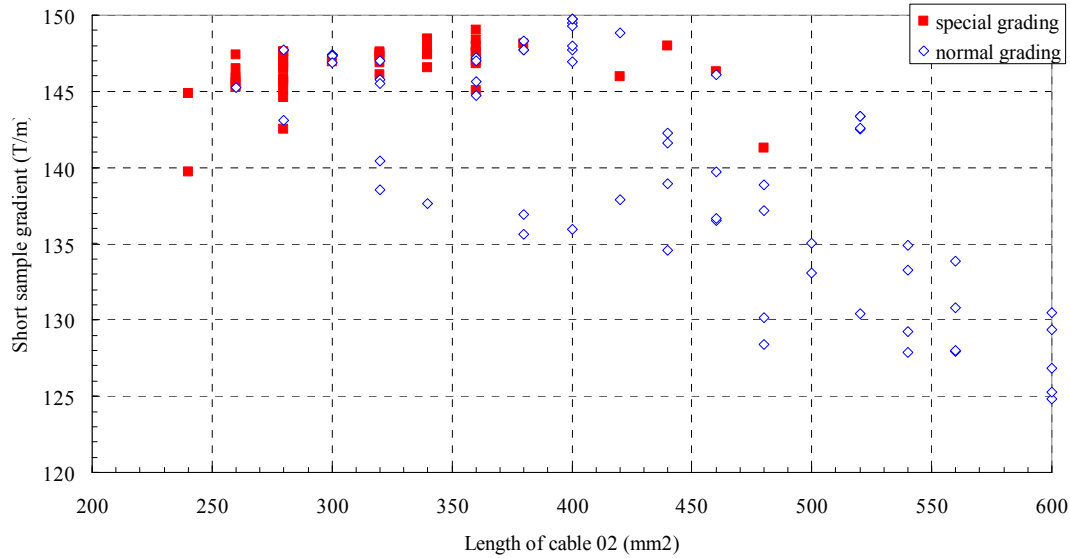


Fig. 10- Short sample gradient versus the length of the cable 02 needed to wind one pole (head excluded) for the normal grading case (empty markers) and for the special grading case (red marker).

The MQXC quadrupole should also have an operational current smaller than 14 kA, which is the present available hardware. In Fig. 11 is plotted the short sample gradient versus the short sample current. The maximal short sample gradient is of 150 T/m and is obtained for a current of 15 kA. Taking a 20% margin, this provides a nominal current of 12 kA, fitting the power supply constraint. In Fig. 12 we also plot the number of turns of cable 01 and cable 02 versus the short sample gradient. We see that to reach the highest gradient the number of turns of cable 01 and cable 02 tends toward similar values of 15-20 turns.

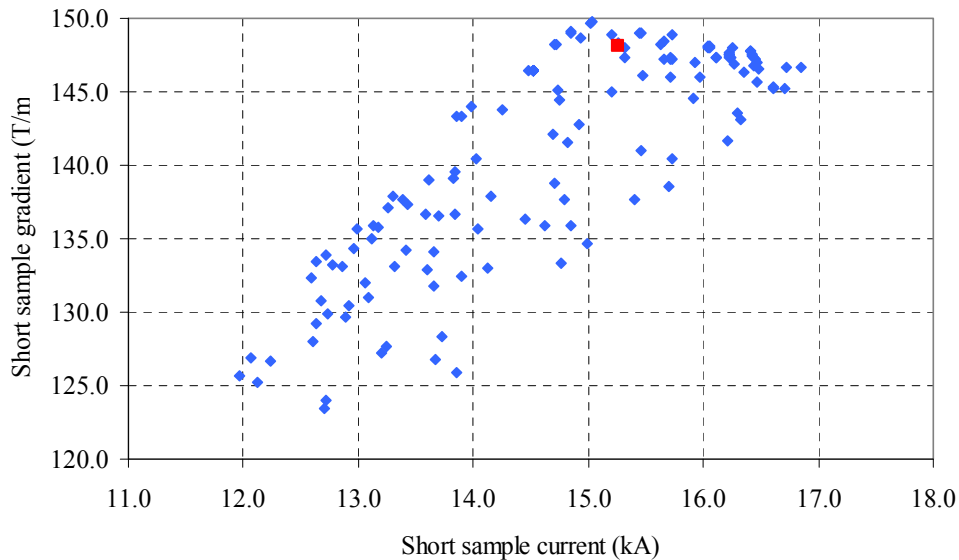


Fig. 11 – Short sample gradient versus short sample current. The red marker is the cross-section we choose for the MQXC quadrupole (see section below).

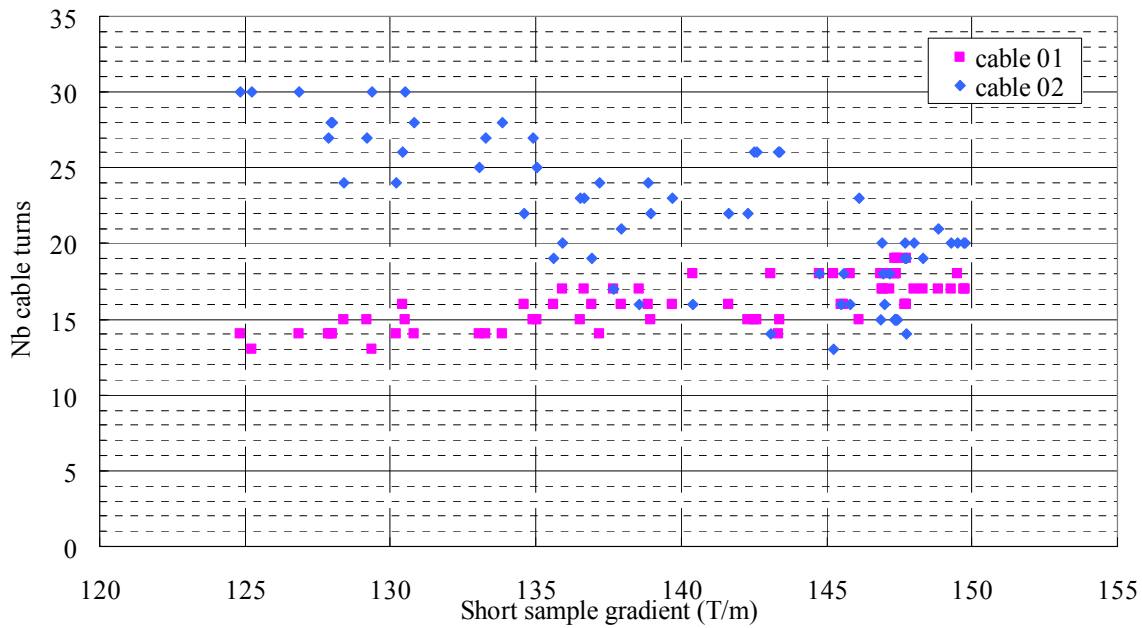


Fig. 12- Number of turns of cable 01 (red markers) and cable 02 (blue markers) versus short sample gradient.

Another parameter which can be computed by means of the Fourier series is the electromagnetic forces acting on the quadrupole coils. In Fig. 13 we plot the vertical and horizontal magnetic forces acting on half a coil considering magnets nominal current. We see that the force  $F_x$  pushing the coil outward is around 1 MN/m and depends barely on the gradient while the vertical force  $F_y$  which compresses the coil at the mid-plane increases continuously with the gradient from 1.2 to 1.4 MN/m. There is not any cross-section providing both a high gradient and low magnetic forces.

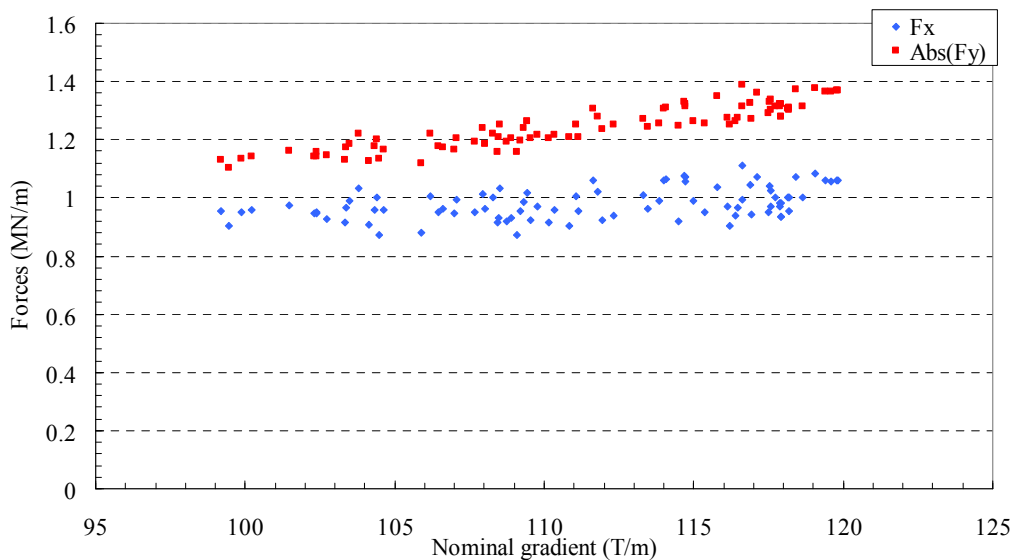


Fig. 13- Vertical and horizontal forces applied on half a magnet coil. The current is set at its nominal value.

#### 2.4. Cross-section with Rutherford cables and iron

Some promising cross-sections based on sector coil were chosen from Fig. 11, in the region of high gradient and for a short sample current around 15 kA, and were realized using the LHC main dipoles cables. To pass from an analytical solution which consists into a set of angles to a coil made

of Rutherford cables, we first compute for each coil block the number of turns of cable which best fits with the sector coil angles. Then, the unavoidable field harmonic distortion due to the discrete cable size and its slight variation from a purely radial sector block are compensated by tuning the block positions and allowing small blocks tilts. The optimization is done through sensitivity matrices built around the first guess. The analysis was carried out with Roxie [11] to take into account also the saturation of the iron yoke at nominal current. The coil cross-section made of pure sector blocks we selected based on the sector coil analysis is sketched in Fig. 14 (left) and is identified in Fig. 11 by a red marker. The coil cross-section made up of real cables and fitting the best the calculated angles is shown in Fig. 14 right. The choice of the coil cross-section among that one maximizing the short sample gradient has been done to have radial blocks, and sufficiently large wedges for easy manufacturing and assembly.

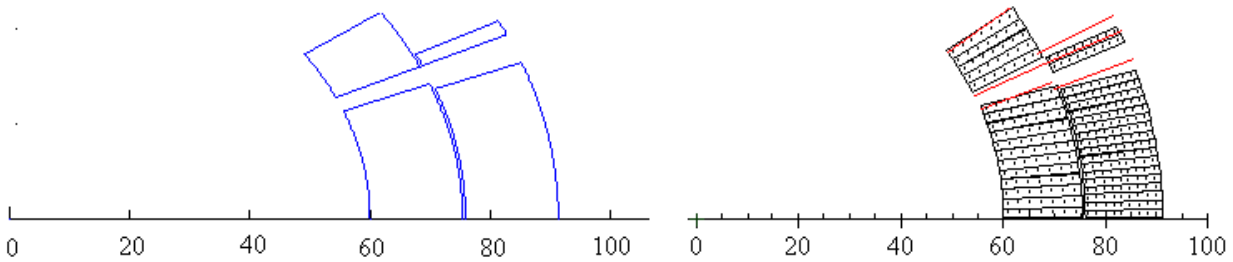


Fig. 14 – MQXC coil cross-section made of pure sector blocks (left) and cross-section made of real cables and fitting the best the pure sector block angles (red lines).

The proposed cross-section of the MQXC coil is presented in Fig. 15 and its main features are summarized in Table 2. The short sample gradient is of 147.1 T/m for a short sample current of 15900 A (iron yoke saturation included). The nominal current taken with 20% operational margin from the short sample current is 12720 A, corresponding to an operational gradient of 118.5 T/m. The iron yoke contribution to the short sample gradient is of 3.3%. For a fixed current, the yoke contribution to the gradient, excluded saturation, is of 12%. When the real geometry of the iron is taken into account, together with iron saturation, these values are reduced to 2.5% and 9% respectively.

The proposed two-layer coil is made of four blocks, and requires 17 turns of cable 01 for the inner layer and 19 turns of cable 02 for the outer layer. This corresponds to ~340 m of cable 01 and ~380 m of cable 02 for a 10-m magnet (ends excluded), that fits well the constraint on the cable length coming from the LHC dipoles (460 and 780 m respectively, (see section 2.1)). The top angle of the coil, given by the pole angle of the inner layer (see Fig. 15), is at 35°. This provides an azimuthal nose length of 21 mm. The thicknesses of the inner edges of the copper wedge located in the inner and outer layer are 4.4 mm and 2.6 mm respectively: this is larger than what we have for the thinnest copper wedge nose of the LHC main dipole (0.5 mm). The inner edge of the block 4 is totally in contact with the copper wedge of the inner layer.

The inner and outer coil are separated by a 0.5 mm thick insulation layer (see Fig. 17), and a 0.12 mm thick ground insulation (instead of 0.125 mm because of the compression of the mid-plane) to the inner and outer layers is set at the mid-plane together with an additional layer, acting as a shim, of 0.1 mm. An additional insulating layer of 0.025 mm is set at the mid-plane of the outer layer and runs along the inner radius of the outer layer over few millimetres. Its role is to improve electrical insulation between layers. The total thickness of the mid-plane is therefore 0.220 mm for the inner and 0.245 mm for the outer layer. A compression of 0.005 mm of the mid-plane is taken into account. The 0.1 mm shims can be used to fine tune the field quality during the magnet production without modifying the coil design. Similar shims can be used between the collar and the coil pole.

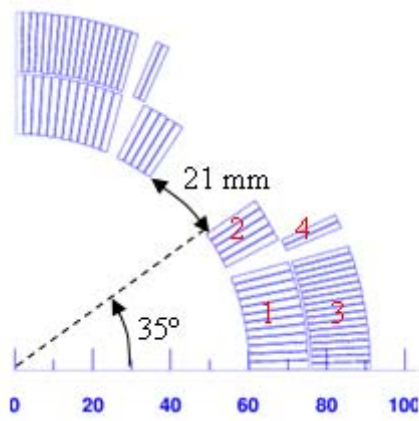


Fig. 15- Proposed cross-section of the MQXC magnet.

Table 2: Geometric parameters of the coil

Block N°	Nb Cond	r (mm)	$\varphi$ (°)	$\gamma$ (°)	cable type
1	12	60.000	0.2101	0.000	cable 01
2	5	60.000	25.728	27.757	cable 01
3	17	75.920	0.1849	0.000	cable 02
4	2	75.920	23.501	22.762	cable 02

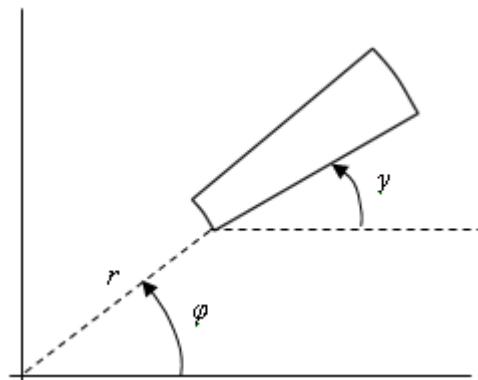


Fig. 16 - Definition of the parameters used in Table 2

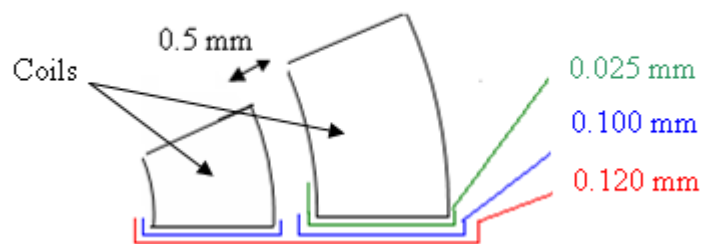


Fig. 17- Scheme of the midplane insulation and shims

## 2.5. Iron yoke

The role of the iron yoke is mainly to shield the magnet from outside magnetic field and to reduce the operational current; it also slightly increases the short sample gradient. The guidelines for the mechanical design aim at having a complete support of electromagnetic forces through the stainless steel collars [6]. This concept has the advantage of decoupling the mechanical design of the collared coils from the magnet yoke. An extensive study has been made to determine the needed thickness of the collars, based on their deformation in nominal conditions [6]: the final value of the thickness has been set to 35 mm. Taking also into account a 2-mm-gap between collars and the iron yoke this provides a yoke inner diameter of 260 mm. Its outer diameter is set at 550 mm for tooling and tunnel limited space reasons. The yoke is a stack iron sheet whose thickness has not yet been defined. For the computation we assumed values similar to the LHC main dipoles, i.e., an iron sheet thickness of 5.8 mm with a package coefficient of 0.985.

The heat exchanger has to fit in the yoke. Two possible configurations for the heat exchanger have been studied [6]. The first configuration needs two 80 mm diameter exchangers, and the second one needs one 105 mm diameter exchanger. The yoke must anyway have four holes to satisfy the four-fold symmetry of the magnet, thus avoiding unallowed multipoles. One has two possible angular positions, i.e., on the midplane or at 45° (see Fig. 18). From the integration point of view, the best choice would be one exchanger, and four holes of 105 mm in line with the mid-plane, but one has also to consider the field quality and the impact on the transfer function. The decrease of the short sample gradient of the 45° and of the 90° solution is around 0.40 % and 0.52 % respectively.

The reduction of the transfer function at nominal current due to the iron saturation with the holes, is 1.5-3%, i.e., in between what we have for the LHC MQXA (6%) and MQXB (2%) (see Fig. 20) and is considered as acceptable. The impact on  $b_6$  is 1-2 units (see Fig. 20). For both solutions the position affecting less the multipole  $b_6$  is the holes in line with the mid-planes. The impact on  $b_{10}$  and  $b_{14}$  is within 0.1 units in all cases.

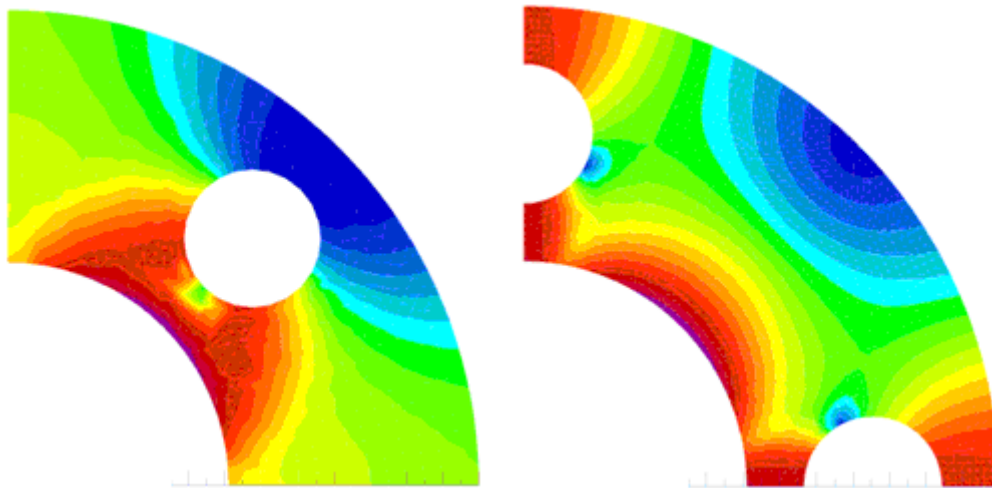


Fig. 18 – Cross-sectional view of the MQXC iron yoke with either 4 holes in line with each pole (left) or 4 holes in line with each mid-plane. The configuration presented here is the 80 mm one.

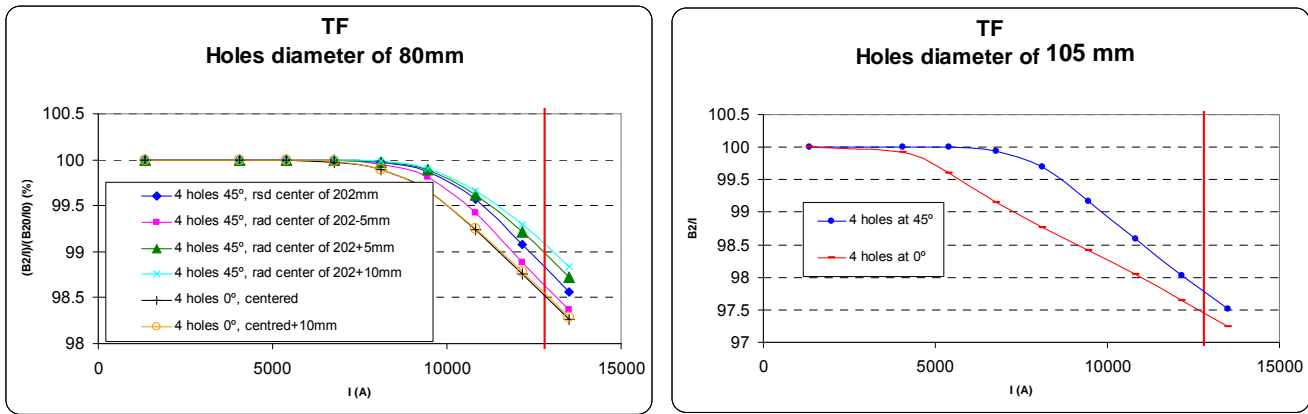


Fig. 19- Transfer function in case of the 80 mm and 110 mm hole cases.

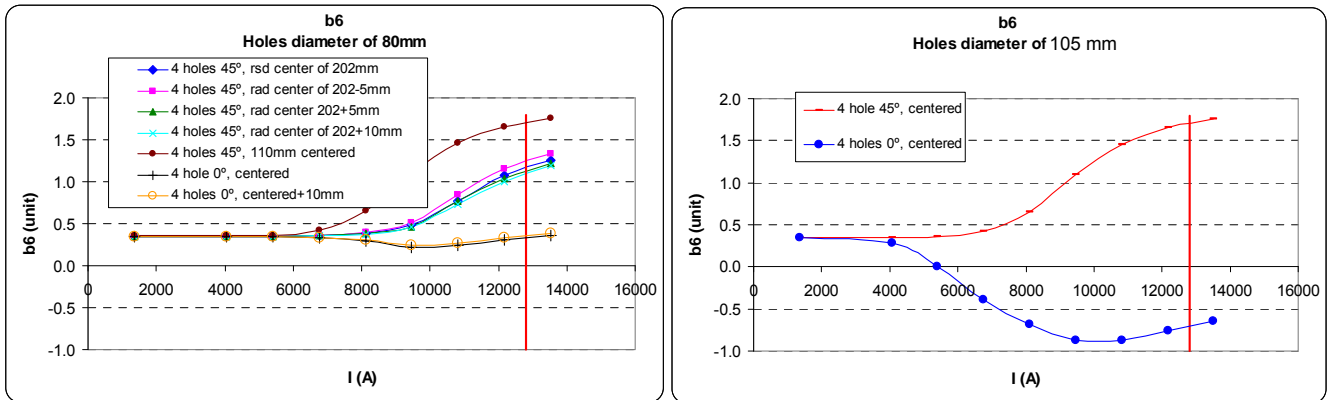


Fig. 20- Study of the impact of holes of 80 mm (left) and 105 mm (right) in the iron yoke on the multipole  $b_6$ . The vertical red line corresponds to the nominal current. The coil cross-section used here was a previous version of the MQXC.

The proposed solution is the 105 mm holes aligned with the mid-planes since this is the best configuration for the cooling system and looks as acceptable form the magnetic point of view. The cross-section of the yoke is shown in detail in Fig. 21. The 105 mm holes are radially centred in the yoke in order to leave 20 mm of matter on each side. A notch (A) is set on the inner radius for the stainless-steel key which allows centring coils and collars assembly in the yoke and another one (B) is set on the outer radius to handle the magnet. Cavities of 20.5 mm diameter (C) used to house the axial iron rod are located on each pole line. Their radial location, still not defined, has to be chosen according to mechanical reasons since their impact on the field quality and on the transfer function is negligible.

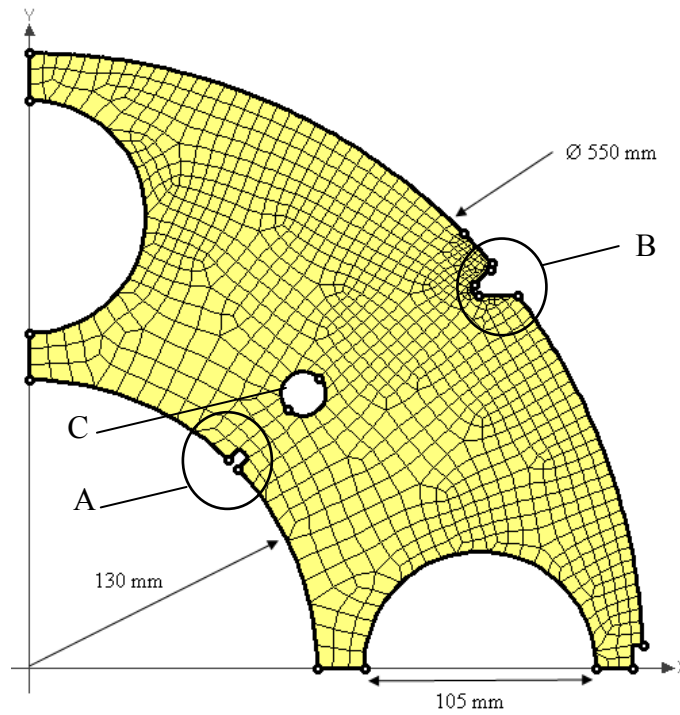


Fig. 21 - Final cross-section of the iron yoke.

## 2.6. Summary of magnetic performances

The final performances of the MQXC quadrupole are summarized in Table 3. The short sample gradient is of 147.1 T/m and the nominal gradient computed at 80 % of the short sample current is of 118.5 T/m. Allowed multipoles are within 0.1 units at nominal current.

Table 3 – Main features of the MQXC magnet

	unit	MQXC
Aperture diameter	mm	120
Inner iron diameter	mm	260
Outer iron diameter	mm	550
Short sample Gradient	T/m	147.1
Short sample current	kA	15.9
Operational gradient	T/m	118.5
Operational current	kA	12.72
Inductance	mH/m	5.06
Reference radius	mm	40
$b_6$ (I = In)	unit	-0.006
$b_{10}$ (I = In)	unit	-0.036
$b_{14}$ (I = In)	unit	-0.076
$F_x$ (I = In)	MN/m	0.93
$F_y$ (I = In)	MN/m	-1.35

Load lines in blocks 1, 2, 3 and 4 (see Fig. 15) are plotted in Fig. 22. The magnet reaches the short sample conditions in block number 2 at a peak field of 9.8 T. Peaks field computed at short sample current in blocks 1, 3 and 4 are 8.8 T, 7.7 T and 8.2 T respectively. The current of the power supply is limited at 14000 A and therefore the MQXC magnet cannot reach on the test bench its short sample current of 15900A. The largest gradient achievable in the tunnel corresponding to a current of 14000 A is of 130 T/m. The effect of the saturation of the iron yoke on the multipoles is shown in



Fig. 24 and the transfer function is plotted, together with the MQXA and MQXB ones. The maximal variation on  $b_6$  is of 0.8 units, and of 0.1 units for  $b_{10}$ .

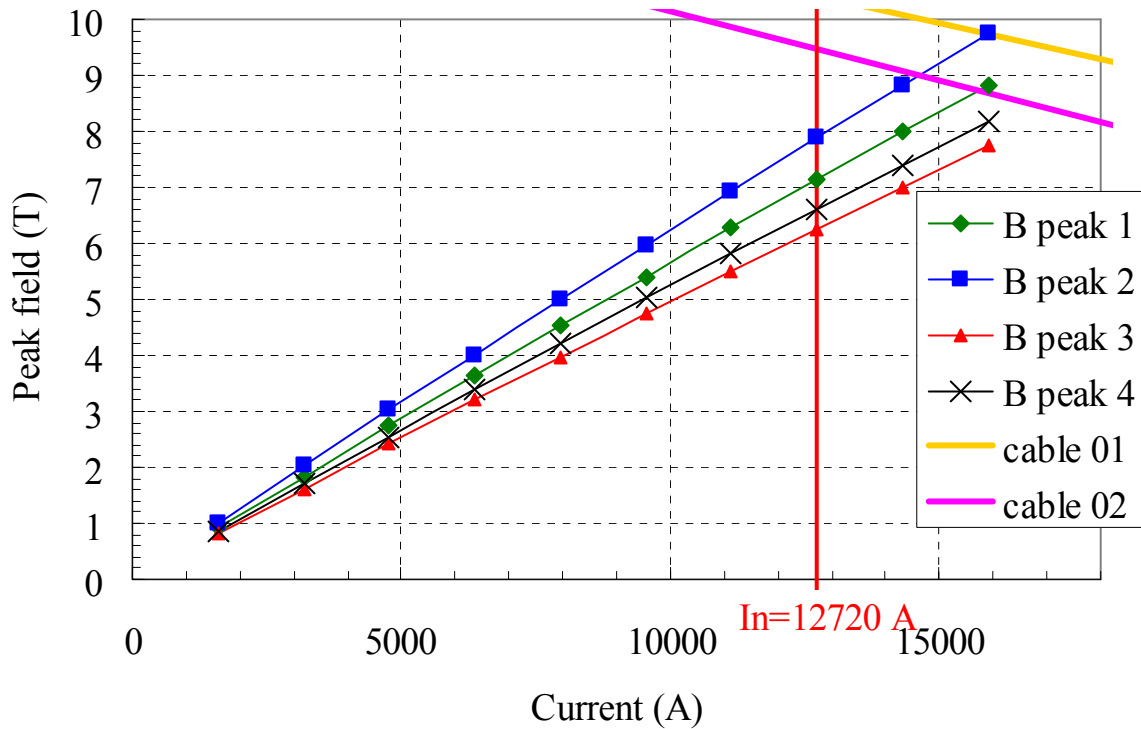


Fig. 22 – Load lines in each of the four coil blocks together with the critical surface of the superconducting cables 01 and 02.

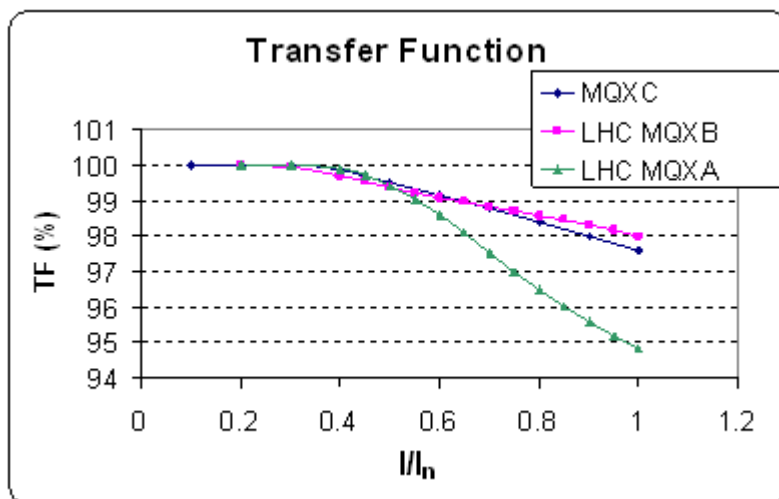


Fig. 23 – Transfer functions of the MQXC, MQXA and MQXB quadrupoles.

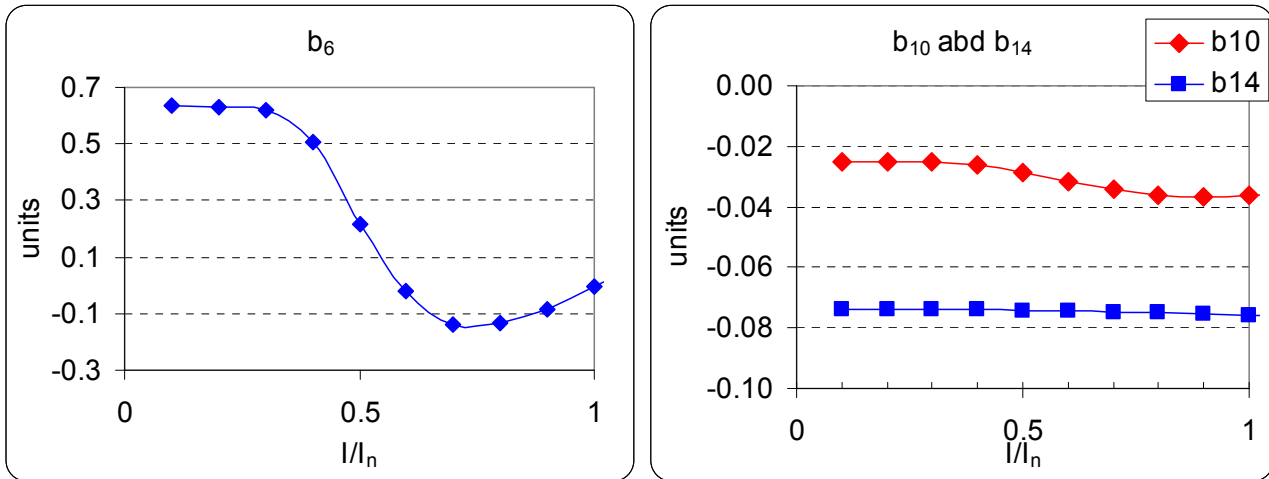


Fig. 24 – Influence of the iron yoke saturation on the multipoles.

### 2.7. Impact on the field quality of a thin slot in the yoke to improve the heat transfer

Here we study the impact on the field quality of a small slot linking the collars to the heat exchanger (see Fig. 25). This could improve the heat transfer but for the moment is only at the stage of study and has not been foreseen to be implemented in the MQXC design. The yoke is symmetric with respect to the  $x$  axis.

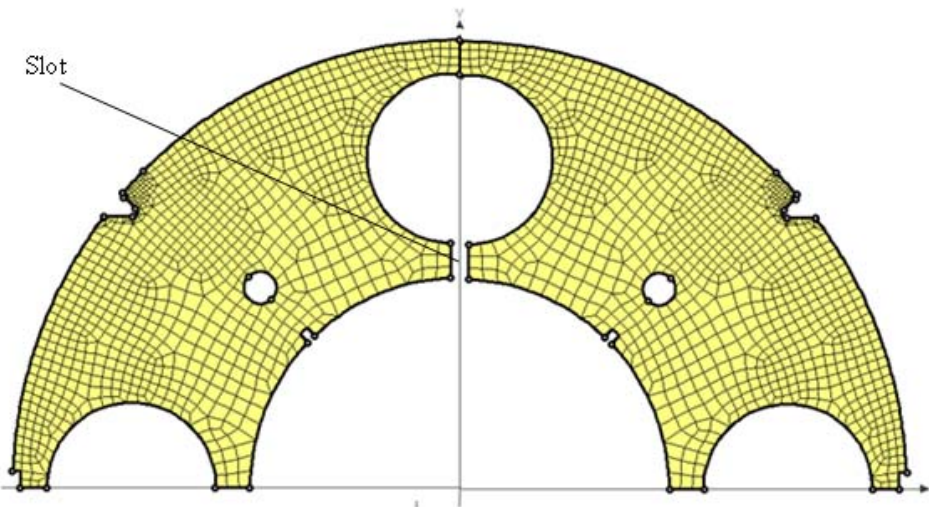


Fig. 25 – Cross-section of the iron yoke. A slot to improve the heat transfer has been implemented.

In Fig. 26 is shown the field harmonic deviation caused by slots in the iron yoke ranging from 1 mm to 3 mm thickness. The case without slot is taken as the reference field harmonic. As expected only  $b_4$ ,  $b_6$ ,  $b_8$  and  $b_{10}$  are marginally affected. Multipoles  $b_4$  and  $b_8$  can be cancelled if the iron sheets are alternatively rotated by  $90^\circ$  so as to get a yoke respecting the four fold symmetry. From the point of view of field quality, this option is viable.

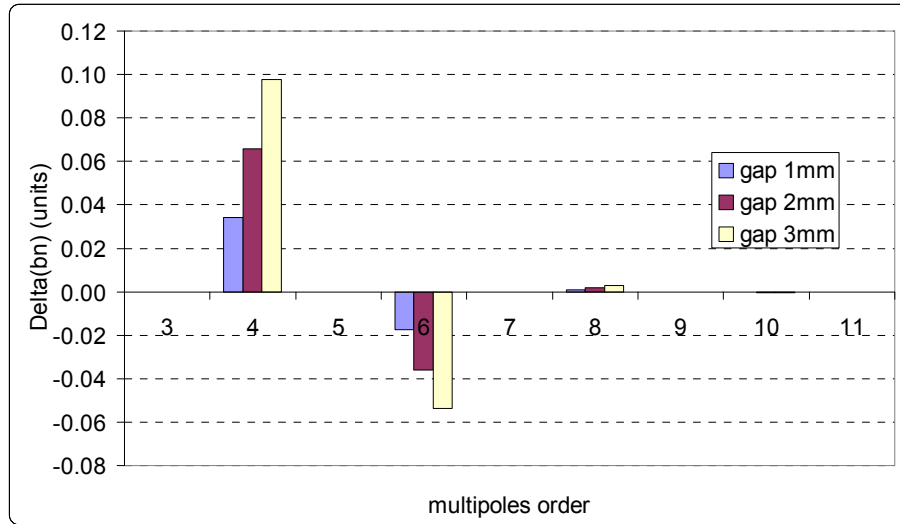


Fig. 26 – Variation of the multipoles due to a small slot of three different thicknesses in the iron yoke. Multipoles reference value is computed when there is no slot.

### III. The layer jump and splice

The layer jump and the splice, sketched in Fig. 27 and in Fig. 28, connect electrically the inner layer to the outer layer and are located close to the connection side of the magnet. Their length is similar to what we have for the LHC main dipole since it is made from the same cable. The inner layer cable is pushed outward (layer jump) and then is overlapped by the outer layer cable (splice). In the splice the current is supposed equally shared between the two cables.

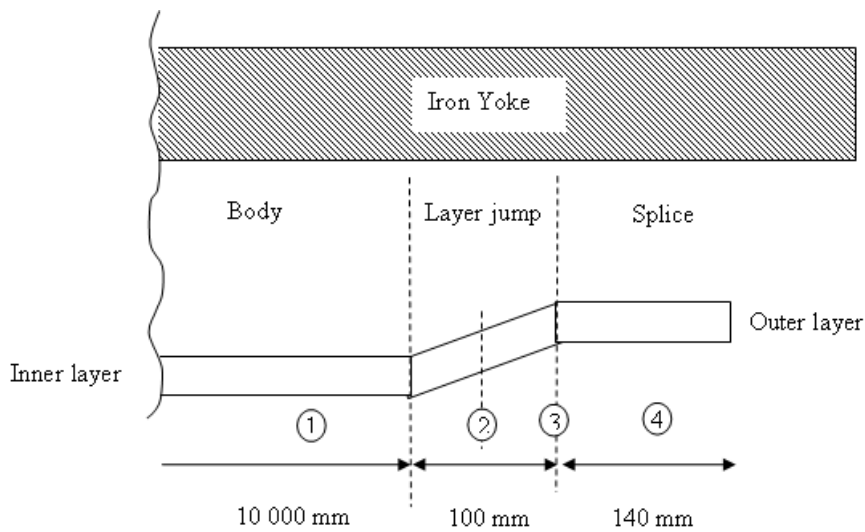


Fig. 27 – Sketch of the layer jump.

In Table 4 we presented the multipoles provided by the layer jump and the associated splice. The field harmonics have been computed at the point 1, 2, 3 and 4 (see Fig. 27). The magnetic length of the layer jump and of the splice is of the same order than the sum of the length of each part i.e. 240 mm. The splice and layer jump contribution to the multipoles integral has been computed assuming a conservative length of the straight part of 7.25 m.

Table 4 – Field harmonics given by the layer jump and the splice and their contribution to the field integral.

Position n	(1)	(2)	(3)	(4)	Contribution to the field integral
$b_6$	-0.01	11.11	16.31	16.10	0.43
$b_{10}$	-0.04	-2.30	-2.97	-2.99	-0.08
$b_{14}$	-0.08	0.13	0.17	0.17	0.00
$a_2$	0.00	35.54	61.38	62.64	1.61
$a_6$	0.00	-5.30	-7.78	-8.29	-0.22
$a_{10}$	0.00	-0.71	-0.92	-0.87	-0.02
$a_{14}$	0.00	0.36	0.42	0.42	0.01
G (T/m)	118.5	118.34	118.23	118.26	118.49

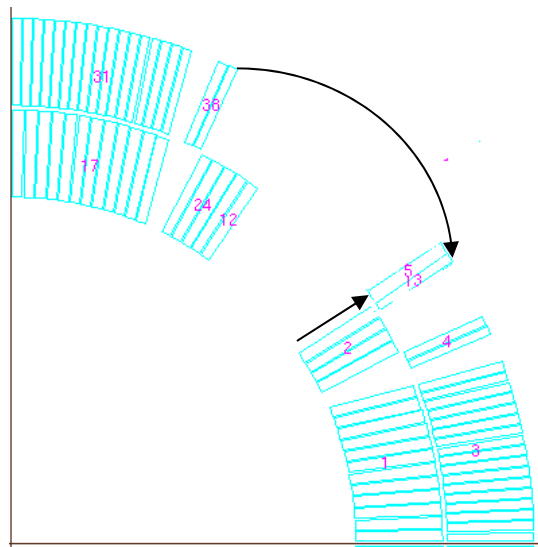


Fig. 28 – Coil block numbering in the splice

## IV. NCS coil end

### 4.1. Geometry of the coil head

Here we present a tentative design of the non connection side of the coil ends. A cross-sectional view in the  $yz$  plan is shown in Fig. 28, and a 3 D view in Fig. 32. We propose to split the four blocks of the coil in six blocks to reduce the peak field (see Fig. 30) while keeping the head as short as possible. The coil head design is based on cables on mandrel and elliptical shape designs, using the code Roxie with the option constant perimeter. The inner and outer edges of the conductor are plotted in Fig. 33. Spacers have been added to the coil end to compensate for keystoneing and adjust the position of each cable in the winding. Their dimensions (see Fig. 31) are similar to what have been measured on the LHC main dipole. The length of the head is of 165 mm.

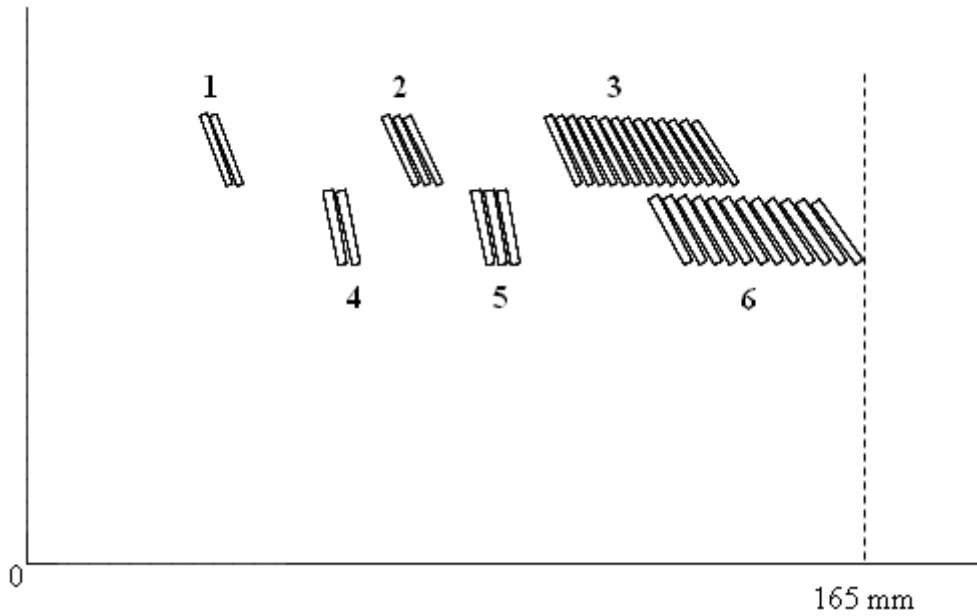


Fig. 29 – Transverse view in the  $zy$  plan of the NCS head coil.

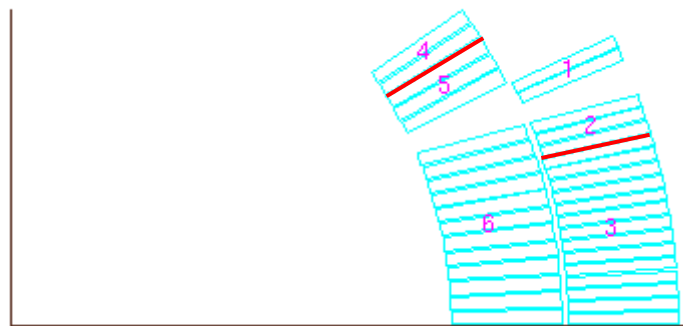


Fig. 30 – Split of the coil blocks leading to the 6 blocks of the coil head.

Ne	Wi	Wo	Hwed	Tend	Etype
1	0.398	0	12.52	4	10
2	0.507	0	17.73	4	10
3	0.507	0	17.73	4	10
4	0.675	0	18.43	4	10
5	0.483	0	33.27	4	10
6	0.688	0	19.84	4	10

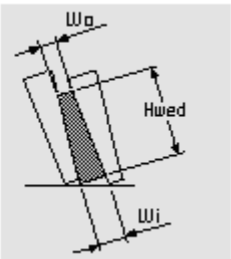


Fig. 31 – Dimensions of the spacers used in the coil end. The numbering corresponds what used in Fig. 29.

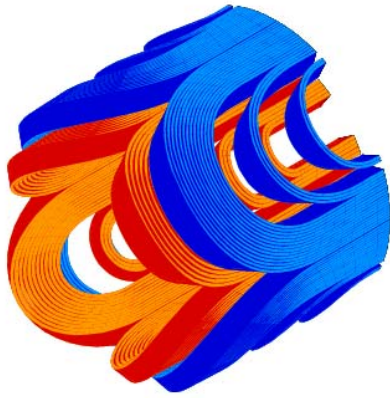


Fig. 32 – 3 D view of the non connection side of the MQXC coil head.

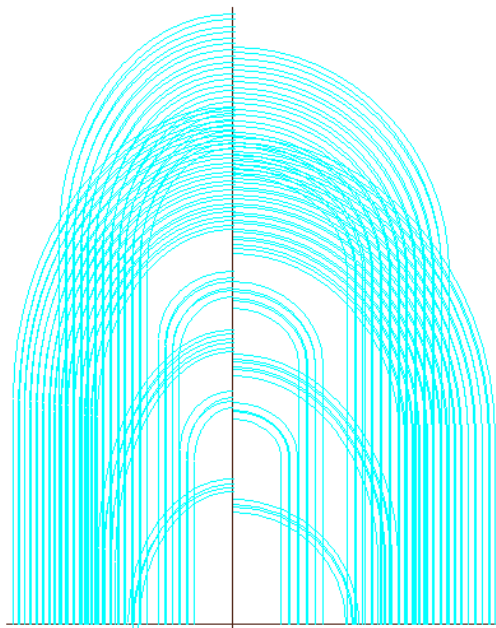


Fig. 33 – Outer and inner edges of the conductors in the  $sz$ -plane.

We first assume an iron yoke much longer than the coil: in this case, the superconductor reaches the critical surface in the head, block 4 in Fig. 30, with a field value very close to what we have in the straight part of the magnet i.e. 9.8 T. This suggests that having the iron covering the heads does not significantly reduce the short sample field, and that this simpler option looks viable.

An alternative option would be to further reduce the peak field in the head, and thus to get the quench in the magnet body, by shortening the iron yoke. In Fig. 34 we plotted the peak field in the coil end versus the difference between the length of the yoke and the length of the coil. Negative  $z$  value means that the yoke is shorter than the coil and positive value means that the yoke is longer than the coil. When  $z = 0$  the yoke edge is in line with the coil edge. Whatever the length of the yoke, the quench is always in block 4 (see Fig. 30), either in the straight part when the yoke is shorter than the coil ( $z < 0$ ) or in the head when  $z > 0$ . If the head is totally naked (i.e. not covered by the yoke), the short sample field in the coil end is 0.2 T lower than in the straight part of the magnet, covered by the yoke, see Fig. 34. This corresponds to  $\sim 0.95$  kA in terms of current margin (see Fig. 35). We remind the reader that the yoke only contributes to 3.2% of the gradient, for a fixed current and an unsaturated yoke, due to the large collars.

Since the margin added by a shorter iron yoke is small, the option of a yoke 50 mm longer than the coil, enabling better shielding of the magnet aperture from external magnetic field, looks

viable (see Fig. 36). In this case, the peak field leading to a quench would be of the same value both in the head and in the straight part, i.e., 9.8 T.

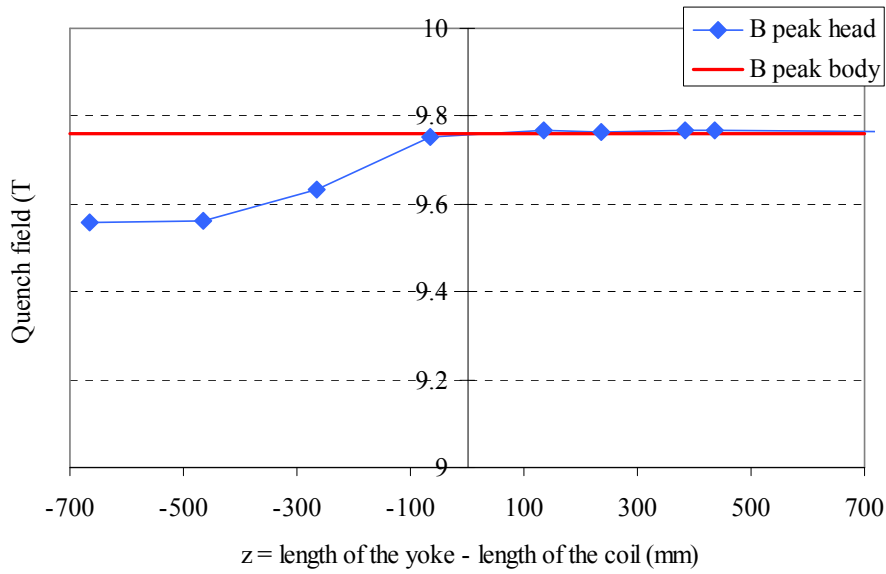


Fig. 34 – Peak field leading to a quench in the coil head (blue line) versus the difference between the length of the yoke and the length of the coil. The red line shows the quench field in the straight part of the magnet.

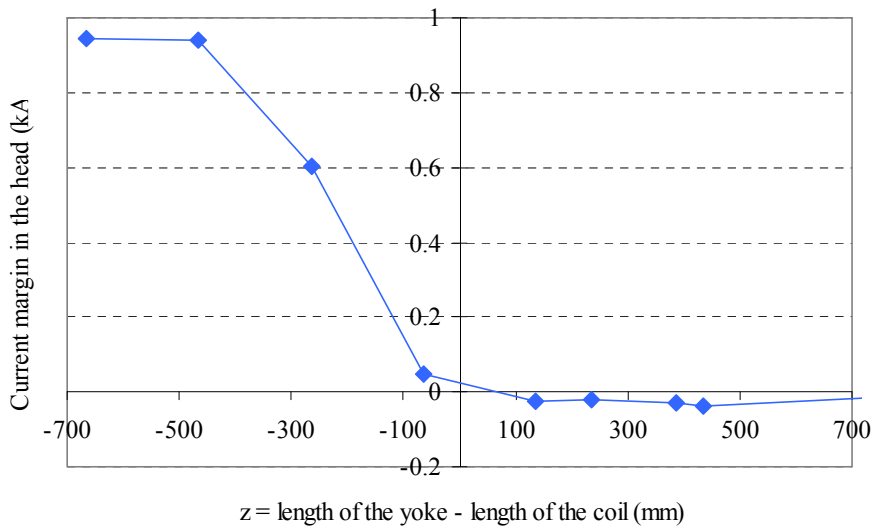


Fig. 35 – Current margin in the coil head versus the difference between the length of the iron yoke and the length of the coil.

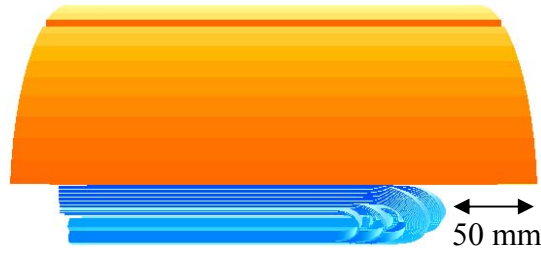


Fig. 36 – Iron yoke and coil in the final configuration: the yoke is 50 mm longer than the coil.

The gradient and the field harmonics along the magnet axis are plotted in Fig. 37. The magnetic length of the head is of 113 mm i.e. 52 mm smaller than the physical length. Average values of the field harmonic are shown in Table 5, together with the harmonic contribution of the head to the integral, which is negligible: the head is rather close to be self compensated. The contribution to the integral is less than 0.1 units.

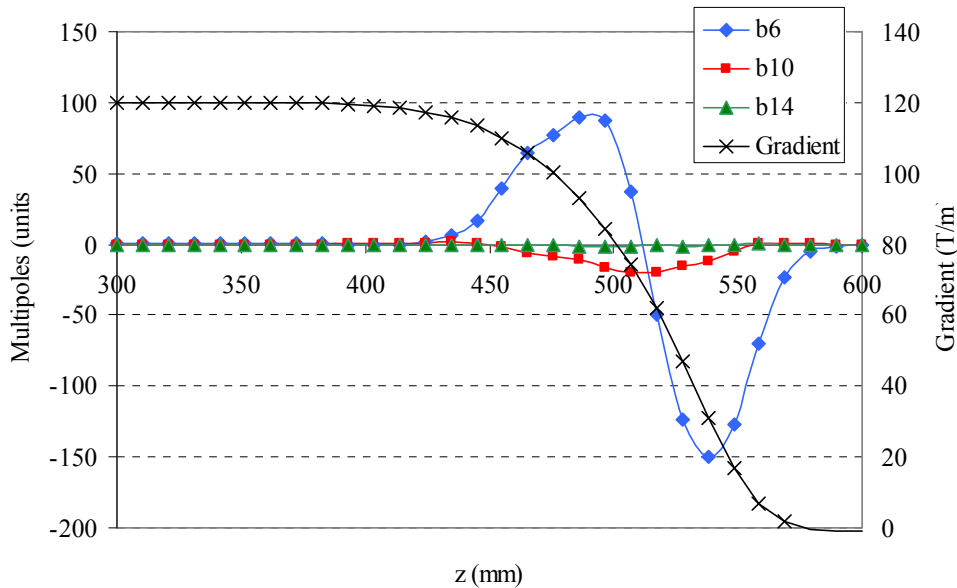


Fig. 37 – Gradient and allowed field harmonics along the axis of the magnet. The iron yoke covers the magnet head.

Table 5 – Average multipole values in the coil end NCS and contribution to the field integral.

	Average over the head	Contribution to the integral
$b_6$	-6.5	-0.10
$b_{10}$	-5.5	-0.08
$b_{14}$	-0.4	-0.01

## V. Field quality

The magnetic field harmonics error of a set of magnets can be defined by two components: The average and the standard deviation. Design values can be always set to zero with an appropriate choice of the coil lay-out. The measured average over a series of magnet is different from zero due to the limited precision of the model (neglected effects), and to systematic errors in the components



or induced by the magnet assembly. This gives a range, called uncertainty, where the systematic is placed. The standard deviation of the field harmonic error is due to the non-reproducibility of the industrial process of the coil manufacturing and assembly. In the following chapter we will estimate the field quality, assuming a 7250-mm-long straight part.

### 5.1. Random component

The position of the coil is the main source of the random component. Random displacements of coil blocks generate the rms component of the field harmonic errors. In [9], the measured standard deviation of the multipoles computed from a set of identical magnets is used to estimate the actual rms blocks displacement  $d$  by means of an inverse Monte-Carlo analysis. Values of rms blocks displacement estimated in [9] for CERN LHC magnets are given in Table 6. They range from 0.010 mm for the MQXA quadrupole to 0.029 mm for the MQ quadrupole. The LHC main dipole, which uses the same cables than the MQXC quadrupole, has a coil block displacement estimated at 0.025 mm.

Table 6 – Estimation of the rms coil blocks displacement in several LHC magnets.

LHC quads	d (mm) ( $1\sigma$ )
MQ	0.029
MQY	0.025
MQXA	0.010
MQXB	0.016
LHC dipole	d (mm)
Main dipole	0.025

Here, we assume that  $d$  does not depend on the magnet aperture as it has been suggested in [10], and we consider the conservative estimate of 0.030 mm. This allows us, by means of a Mont-Carlo analysis, to estimate the field harmonic error caused by random movements of the blocks of 0.030 mm. Obtained results are presented in Table 7 and are plotted in Fig. 38. As expected  $\sigma_{an} = \sigma_{bn}$ . For  $b_6$ , the experience shows that the spread in the position is much larger than what provided by the other multipoles. The spread in the coil position for the MQ associated to  $b_6$  is 0.080 mm. We used this value to estimate  $\sigma_{b6}$  in our case.

Table 7 – Multipoles standard deviation given at  $1\sigma$  cause by a rms coil blocks displacement of 0.030 mm. The reference radius is taken as  $2/3$  of the aperture radius.

n	Std. dev. (unit) ( $1\sigma$ )	
	bn	an
3	0.89	0.89
4	0.64	0.64
5	0.46	0.46
6	1.28	0.33
7	0.21	0.21
8	0.16	0.16
9	0.08	0.08
10	0.06	0.06
11	0.03	0.03
12	0.02	0.02
13	0.01	0.01
14	0.01	0.01

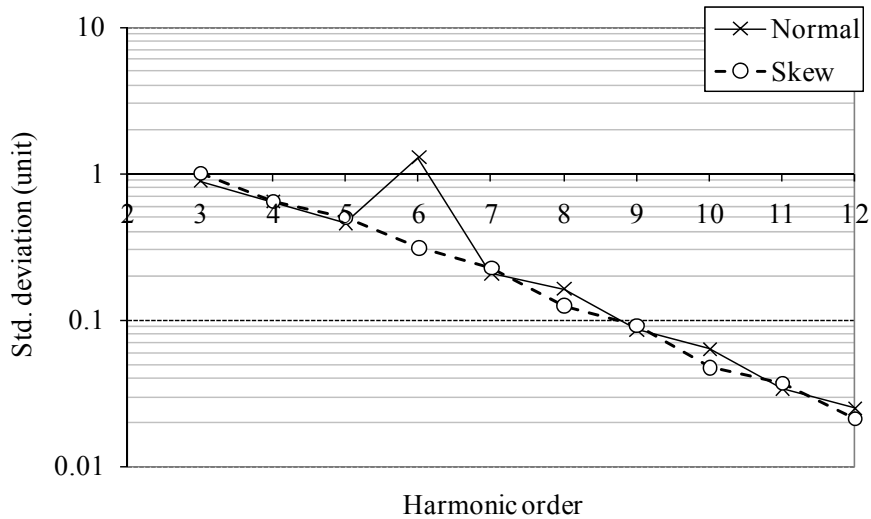


Fig. 38 – Harmonic standard deviation caused by a random displacement of the blocks of rms value of 0.029 mm.

## 5.2. Systematic field harmonic errors

In this chapter we compute the variation of the systematic field harmonics that can be induced by systematic imperfections in the components. Computations have been performed at nominal current (12.7 kA) and at 2/3 of the aperture radius (40 mm).

### 5.2.1. Alignment

A 0.1 mm misalignment of the quadrupole creates 25 units of  $a_1$  or  $b_1$ . The rest of the feed-down effects are negligible.

### 5.2.2. Yoke ellipticity

We assume an error in the yoke fabrication leading to an elliptical shape. The parameter on which we play is the dimension  $x$  shown in Fig. 39. The magnetic field error induced by a variation of  $x$  of  $\pm 0.1$  mm is summarized in Table 8.

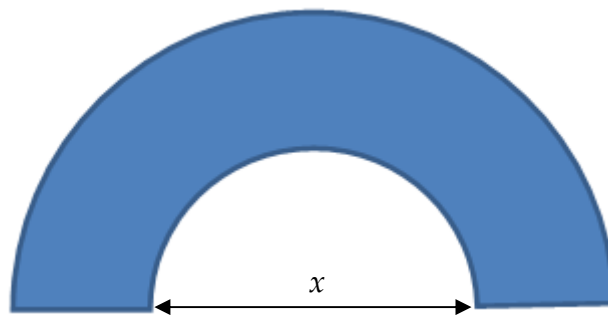


Fig. 39 – Parameter  $x$  on which we play to shape the yoke like an ellipse.

Table 8 – Field error due to an elliptical shape of the inner radius of the iron yoke

	$x=-0.1$ mm	$x=+0.1$ mm
$\Delta b_4$	-0.05	0.04
$\Delta b_6$	0.00	0.00
$\Delta b_{10}$	0.00	0.00
$\Delta b_{14}$	0.00	0.00

### 5.2.3. Coil misplacement within the yoke

The impact of a misalignment of the coil with respect to the yoke is shown in Table 9.

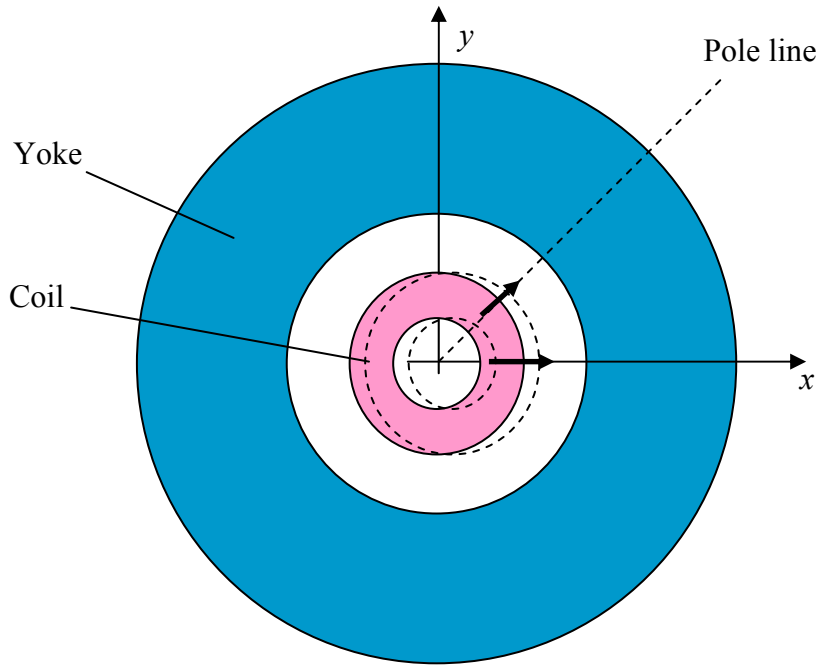


Fig. 40 – Radial shift of the quadrupole coil inside the iron yoke. The dashed donut shows a shift of the quadrupole in the x direction.

Table 9 – Field error due to a radial shift of the quadrupole coil.

order	+0.1 mm in x	-0.1 mm in x	+0.1mm @ pi/4		-0.1mm @ pi/4	
	$\Delta b_n$	$\Delta b_n$	$\Delta b_n$	$\Delta a_n$	$\Delta b_n$	$\Delta a_n$
3	0.46	-0.46	0.33	-0.33	-0.33	0.33
4	0.00	0.00	0.00	0.00	0.00	0.00
5	0.00	0.00	0.00	0.00	0.00	0.00

### 5.2.4. Radial position of collars

A systematic error of +/- 0.05 mm on the collar inner radius, as shown in Fig. 41, gives the field harmonics shown in Table 10.

Table 10 – Field error due to a decrease/increase of the collar radius

	collar radius +/-0.05mm	
	+0.05 mm	-0.05 mm
$\Delta b_6$	0.63	-0.63
$\Delta b_{10}$	0.02	-0.02
$\Delta b_{14}$	0.00	0.00

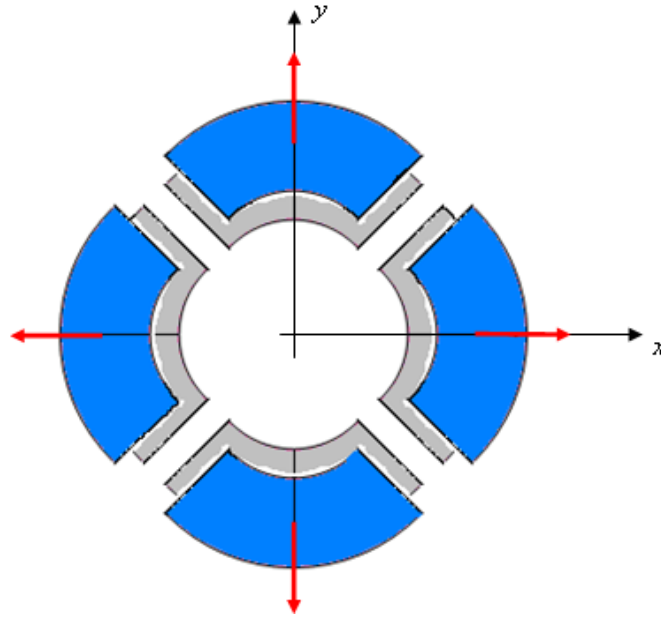


Fig. 41 – Shift of the coils along the x and y axis.

### 5.2.5. Defect on the collar nose thickness

We consider a defect on the collar nose azimuthal thickness of  $\pm 0.05$  mm. The cable insulation is either compressed or relaxed while the copper wedge is assumed infinitely rigid.

Table 11 – Effect of a variation of  $\pm 0.05$  mm of the azimuthal length of the collar nose

	+0.05 mm	-0.05 mm
$\Delta b_6$	1.10	-1.10
$\Delta b_{10}$	-0.10	0.10
$\Delta b_{14}$	0.02	-0.02

### 5.2.6. Ellipticity of the collar

Assembly and electromagnetic forces can lead to a collar deformation. These forces may tend to re-shape the collar as shown in Fig. 42. The effect of a coil deflection of 0.05 mm on the multipoles is given in Table 12.

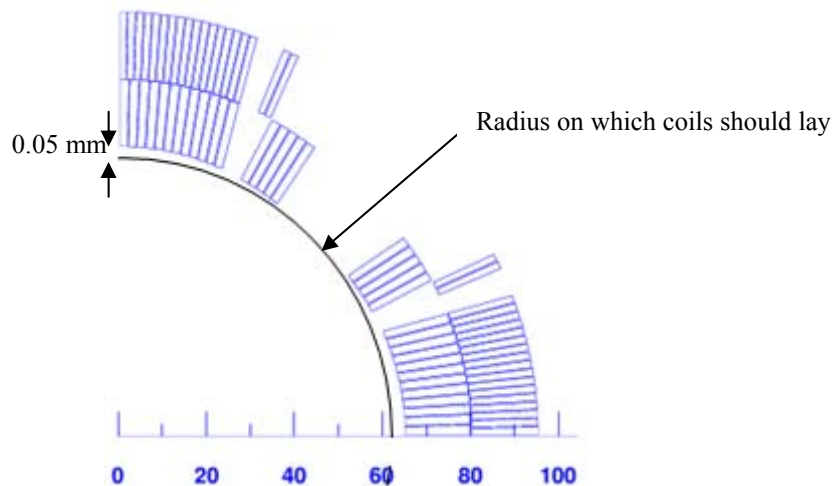


Fig. 42 – Deflection of the coil from its initial shape due to bursting Lorentz forces.

Table 12 – Effect of a coil deflection of 0.05 mm on the field quality.

$\Delta b_6$	0.28
$\Delta b_{10}$	0.04
$\Delta b_{14}$	-0.002

### 5.2.7. Collars permeability

The variation of the multipoles due to a variation of the collar relative permeability of 1.003 +/- 0.002 (tolerances specified for LHC magnets) is shown in Table 13. At this early step of the design the collar shape has not been chosen. For the computation we assume that it fits with the coil border as shown in Fig. 43.

Table 13 – Effect of the collar permeability on the field harmonic. Harmonics reference value are taken for  $\mu_r = 1.003$ .

$\mu_r$	1.001	1.005
$\Delta b_6$	0.70	-0.70
$\Delta b_{10}$	-0.08	0.08
$\Delta b_{14}$	0.01	-0.01

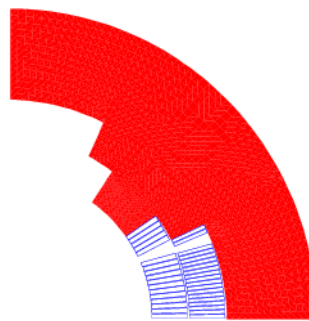


Fig. 43 – Cross-section of the collar used to estimate the effect of a variation of its permeability on the field harmonics.

### 5.2.8. Copper wedges defect

We consider two different types of copper wedges defects: the first one (see Fig. 44 left) is an error of +/- 0.05 mm on the copper wedge azimuthal thickness, the second one (see Fig. 44 right) is an increase/decrease of the keystone angle corresponding to a variation of +/- 0.05 mm of the inner edge and of -/+ 0.05 mm of the outer edge. The related field errors are given in Table 14 and Table 15. The dimension of the collar nose was kept constant and thus the cables insulation thickness had to be adjusted.

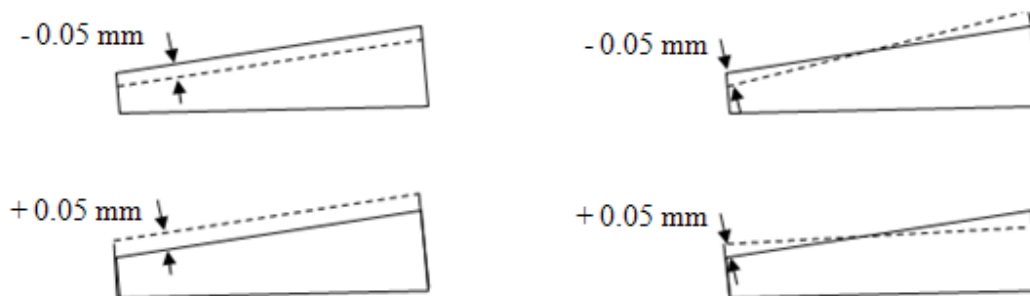


Fig. 44 – Copper wedge imperfections.

Table 14 – Field error due to change in the copper wedge azimuthal thickness

copper wedges +/- 0.05 mm az								
	cp1+/cp2 0	cp1-/cp2 0	cp1-/cp2-	cp1-/cp2+	cp1 0/cp2+	cp1 0/cp2-	cp1+/cp2-	cp1+/cp2+
$\Delta b_6$	0.78	-0.78	-1.0	-0.47	0.32	-0.32	0.47	1.10
$\Delta b_{10}$	0.08	-0.08	-0.10	-0.07	0.02	-0.02	0.07	0.10
$\Delta b_{14}$	-0.02	0.02	0.02	0.02	0.00	0.00	-0.02	-0.02

Table 15 – Field error due to change in the copper wedge keystone angle

copper wedges +/- 0.05 mm tilt								
	incp1-/cp20	incp1+/cp20	incp1+/cp2+	incp1+/cp2-	incp1-/cp2-	incp-/cp2+	incp10/cp2+	incp10/cp2-
$\Delta b_6$	-0.00	0.02	-0.00	0.03	0.02	-0.02	-0.02	0.02
$\Delta b_{10}$	-0.11	0.11	0.11	0.10	-0.11	-0.10	0.00	-0.00
$\Delta b_{14}$	0.025	-0.025	-0.025	-0.025	0.025	0.025	0.00	0.00

### 5.2.9. Errors in the curing mould

Here we deal with imperfections in the curing mould resulting in coil blocks radial misplacements. We assume that only one coil over eight is affected. Normal and skew harmonics resulting from a radial displacement of + 0.05 mm (see Fig. 15) are given in Table 16.

Table 16 – Polymerisation defect (radial displacement of + 0.05 mm).

order	block 2		block 1		block 1/2/3		block 2/4	
	$\Delta an$	$\Delta bn$	$\Delta an$	$\Delta bn$	$\Delta an$	$\Delta bn$	$\Delta an$	$\Delta bn$
2	-1.24		-1.27		-3.4		-1.46	
3	0	0	0	0	0	0	0	0
4	0	0.01	0	0.01	0	0.04	0	0.01
5	0	0	0	0	0	0	0	0
6	0.03	-0.55	-0.99	0.40	-1.27	0.01	0.00	-0.59
7	0	0	0	0	0	0	0	0
8	0	0	0	0	0	0	0	0
9	0	0	0	0	0	0	0	0
10	0.1	0.07	-0.14	-0.06	-0.06	0.00	0.1	0.07
11	0	0	0	0	0	0	0	0
12	0	0	0	0	0	0	0	0
13	0	0	0	0	0	0	0	0
14	-0.021	0.009	-0.004	-0.01	-0.025	0	-0.02	0.01

### 5.3. Field error due a radial offset of the splice

Multipoles deviation due a radial offset of the splice of +/- 0.1 mm is shown in Table 17. The magnetic length of the splice (140 mm) is small with respect to the length of the straight part (7.25 m) and the multipoles produced by a shift of +/- 0.1 mm of the splice are also small: we can neglect the splice shift effect on the uncertainty calculation.

Table 17 – Multipoles values due to the splice and multipoles deviation due to a radial shift of +/- 0.1 mm of the splice

n	$\langle b_n \rangle$	$\Delta b_n$		$\langle a_n \rangle$	$\Delta a_n$	$\Delta a_n$
		+	-			
3	0	0	0	0	0	0
4	0	0	0	0	0	0
5	0	0	0	0	0	0
6	16	0.05	-0.05	-8.3	-0.02	0.02
7	0	0	0	0	0	0
8	0	0	0	0	0	0
9	0	0	0	0	0	0
10	-3	0	0	-0.9	0	0
11	0	0	0	0	0	0
12	0	0	0	0	0	0
13	0	0	0	0	0	0
14	0.17	0	0	0.4	0	0

#### 5.4. Field error due to longitudinal displacement of layers

Here we estimate the effect of a longitudinal displacement of +/- 3 mm of one layer coil with respect to the other on the field quality (see Table 18). The magnetic length of the head is of 113 mm. This leads to very small integrated field errors e.g. the integrated  $b_6$ , considering a coil straight part length of 7250 mm, is of 0.01 units. We can therefore neglect this effect in the computation of the uncertainty.

Table 18 – Longitudinal displacement of the outer layer coil.

	average over the head		contribution to integral	
	+3 mm	-3 mm	+3 mm	-3 mm
$\Delta b_6$	0.88	-0.88	0.01	-0.01
$\Delta b_{10}$	-0.03	0.03	0.00	0.00
$\Delta b_{14}$	-0.001	0.001	0.00	0.00

#### 5.5. Magnetic field quality summary

##### 5.5.1. Geometric multipoles values

Contribution of the geometric multipoles produced in the straight part, in the layer jump and in the NCS coil head to the field integral are summarized in Table 19. We considered a straight part of 7250 mm leading to a total magnetic length of 7603 mm (CS coil end is not included). The non-zero values of the harmonic components produced in the heads and the in layer jump has to be compensated through a fine tuning of the cross-section. The impact of the collar permeability, which is ~1 unit on  $b_6$  (see Table 19) and has not been taken in the cross-section design, can also be compensated in a similar way. The fine tuning of the multipoles can be done only when the shape of the collar and the final length of the magnet are known, and when the coil head CS is designed.

Table 19 – Geometric multipoles components: contribution to the field integral.

multipoles	Straight part, Lmag = 7250 mm		Layer jump	Head
	collar with $\mu r=1$	collar with $\mu r=1.003$	Lmag = 240 mm	Lmag = 113 mm
b3	0	0	0	0
b4	0	0	0	0
b5	0	0	0	0
b6	-0.01	-1.02	0.42	-0.10
b7	0	0	0	0
b8	0	0	0	0
b9	0	0	0	0
b10	-0.03	0.07	-0.08	-0.08
b11	0	0	0	0
b12	0	0	0	0
b13	0	0	0	0
b14	-0.07	-0.08	0.00	-0.01
a3	0	0	0	0
a4	0	0	0	0
a5	0	0	0	0
a6	0	0	-0.21	0
a7	0	0	0	0
a8	0	0	0	0
a9	0	0	0	0
a10	0	0	-0.02	0
a11	0	0	0	0
a12	0	0	0	0
a13	0	0	0	0
a14	0	0	0.01	0

### 5.5.2. Uncertainty

The uncertainty has been obtained from the quadratic sum of the multipoles maximum absolute value produced by each defect described in chapter 5.2. Defects meet in the coil end and in the splice are not taken into account because they have a negligible impact on field harmonics.

Table 20 – Uncertainty in the field quality expected in the MQXC quadrupole.

	yoke	collar				copper wedges		mould	Quadratic
	a	b	c	d	e	f	g	h	sum
\Delta b3	0.46	0	0	0	0	0	0	0	0.46
\Delta b6	0	0.63	1.1	0.7	0.28	0.78	0.03	0.60	1.77
\Delta b10	0	0	0.1	0.08	0.05	0.08	0.11	0.06	0.20
\Delta b14	0	0	0.020	0.006	0.002	0.02	0.025	0.010	0.040
\Delta a6	0	0	0	0	0	0	0	1.27	1.27
\Delta a10	0	0	0	0	0	0	0	0.14	0.14
\Delta a14	0	0	0	0	0	0	0	0.025	0.025

- a) Coil displaced with respect to the yoke (section 5.2.3)
- b) Radial displacement of the collar (section 5.2.4)
- c) Defect on the nose thickness (section 5.2.5)
- d) Defect on the collar permeability (section 5.2.7)
- f) Error on the azimuthal thickness of the copper wedges (section 5.2.8)
- e) Collars ellipticity (section 5.2.6)
- g) Error on the keystone angle of the copper wedges (section 5.2.8)
- h) Defect in curing mould (section 5.2.9)



### 5.5.3. Field quality table

In Table 21 is summarized the uncertainty and the random components of the field error. The uncertainty estimate involves only some symmetries. For the other unallowed multipoles, we assume that the uncertainty is equal to the sigma of the random (in italic, in Table 21). *The geometric part at high field can be assumed as zero, since the coil can be fine tuned to correct the collar contribution, etc.* This is why it is not given in the Table. For the injection, the same values can be used since the random geometric by far dominates the random part of the persistent current. The only difference at injection is that the geometric  $b_6$  will be different from zero, i.e. the whole persistent current contribution will be visible. A preliminary computation<sup>1</sup> gives -6 units. Summarizing, all systematic at high field can be taken as zero, the systematic at injection are zero except  $b_6=6$  units, and the uncertainty and random are the same at injection and high field, and are given in Table 21.

Table 21 – MQXC field quality table at high field. The length of the straight part is of 7250 mm and the total magnetic length is of 7603 mm.

	Uncertainty	Random
b3	<i>0.46</i>	0.89
b4	<i>0.64</i>	0.64
b5	<i>0.46</i>	0.46
b6	1.77	1.28
b7	<i>0.21</i>	0.21
b8	<i>0.16</i>	0.16
b9	<i>0.08</i>	0.08
b10	0.20	0.06
b11	<i>0.03</i>	0.03
b12	<i>0.02</i>	0.02
b13	<i>0.02</i>	0.01
b14	0.04	0.01
a3	<i>0.89</i>	0.89
a4	<i>0.64</i>	0.64
a5	<i>0.46</i>	0.46
a6	1.27	0.33
a7	<i>0.21</i>	0.21
a8	<i>0.16</i>	0.16
a9	<i>0.08</i>	0.08
a10	0.14	0.06
a11	<i>0.03</i>	0.03
a12	<i>0.02</i>	0.02
a13	<i>0.01</i>	0.01
a14	0.03	0.01

### 5.6. Fine tuning of the multipoles through mid-plane shims

The discrepancy between the design and the measured values of the allowed harmonics ( $b_6, b_{10}, b_{14}...$ ) can be compensated adding or removing shims at the mid-planes. The expected agreement between model and measurements, mainly due to deformation and systematic effects of the tolerances, has been estimated around 1.8 unit for  $b_6$ , and a fraction of units for the higher orders (see Table 21, uncertainty column). One should have enough flexibility to correct this discrepancy

<sup>1</sup> S. Russenschuck, private communication.

through the mid-plane shims without changing the coil geometry, i.e. the copper wedges or the pole angles.

As shown in Fig. 17 an additional 0.1 mm sheet of insulation, acting as a shim, is initially placed at the mid-plane. We computed the case of a 0.1 mm shim which is added or removed from the mid-plane. The magnet is powered at its nominal current (12720 A) and the multipoles are measured at 2/3 of the aperture radius. Results obtained are summarized in Table 22. Removing shims produce positive multipoles while adding shims produce negative one. With a 0.1 mm shim  $b_6$  can be compensated up to +/- 5 units,  $b_{10}$  can be compensated up to +/- 0.2 units and  $b_{14}$  can be compensated up to +/- 0.1 units.

Table 22 – Impact of a 0.1 mm shim on the field quality

	L1 -0.1 mm L2 -0.1 mm	L1 +0.1 mm L2 +0.1 mm	L1 0.0 mm L2 -0.1 mm	L1 0.0 mm L2 +0.1 mm	L1 +0.1 mm L2 0.0 mm	L1 -0.1 mm L2 0.0 mm	L1 +0.1 mm L2 -0.1 mm	L1 -0.1 mm L2 +0.1 mm
$\Delta b_6$	5.109	-5.122	1.317	-1.321	-3.797	3.796	-2.478	2.478
$\Delta b_{10}$	0.216	-0.217	0.065	-0.064	-0.152	0.152	-0.088	0.087
$\Delta b_{14}$	0.095	-0.095	0.001	-0.001	-0.094	0.094	-0.093	0.093

## VI. Summary

We presented a design for the new inner triplet quadrupole. A two layer cross-section, based on the MB cables with four blocks has 148.1 T/m of short sample gradient, i.e. it provides 118.5 T/m of nominal gradient with 20% margin, or can work at 120 T/m with 19.0% margin. The operational current is 12.8 kA, fitting the present power supply hardware constraints of 14 kA. We presented a novel method to make an exhaustive search of the possible solutions with four blocks. A proposal for the iron yoke, for the layer jump and from the heads non connection side are also made. Estimates of the expected field quality are presented.

## References

- [1] J. P. Koutchouk, L. Rossi, E. Todesco, *LHC Project Report 1000* (2007).
- [2] R. Ostojic, et. al, *LHC Project Report 1163* (2008).
- [3] Y. Ajima, et. al, *Nucl. Instrum. Meth. A 550* (2005) 499.
- [4] M. Lamn, et. al, *European Particle Accelerator Conference* (2006) 2637.
- [5] R. Ostojic, et. al, *Particle Accelerator Conference* (2005) 2797.
- [6] F. Regis, P. Fessia in preparation, and talks given in the LIUWG-14 (2008).
- [7] J. Adam, et al., *IEEE Trans. Appl. Supercond.* **12** (2002) 1056.
- [8] D. Tommasini and D. Richter, *European Particle Accelerator Conference* (2008) 2467.
- [9] L. Rossi, E. Todesco, *Phys. Rev. STAB*, Vol. 9, pp 102401, 2006
- [10] B. Bellesia, et al., *Phys. Rev. STAB* **10** (2007) 062401.
- [11] S. Russenschuck, ed. *CERN Yellow Report 99-02* (1999).